Multiscale modeling of θ' precipitation in Al–Cu binary alloys

V. Vaithyanathan [a,*], C. Wolverton [b], L.Q. Chen [a]

[a] *Department of Materials Science and Engineering, The Pennsylvania State University, University Park, PA 16802, USA*
[b] *Ford Research and Advanced Engineering, MD3083/SRL, Dearborn, MI 48121-2053, USA*
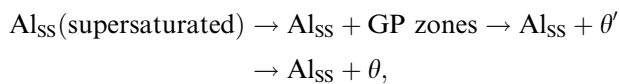
Abstract

We present a multiscale model for studying the growth and coarsening of θ' precipitates in Al–Cu alloys. Our approach utilizes a novel combination of the mesoscale phase-field method with atomistic approaches such as first-principles total energy and linear response calculations, as well as a mixed-space cluster expansion coupled with Monte Carlo simulations. We give quantitative first-principles predictions of: (i) bulk energetics of the Al–Cu solid solution and θ' precipitate phases, (ii) interfacial energies of the coherent and semi-coherent θ'/Al interfaces, and (iii) stress-free misfit strains and coherency strain energies of the θ'/Al system. These first-principles data comprise all the necessary energetic information to construct our phase-field model of microstructural evolution. Using our multiscale approach, we elucidate the effects of various energetic contributions on the equilibrium shape of θ' precipitates, finding that both the elastic energy and interfacial energy anisotropy contributions play critical roles in determining the aspect ratio of θ' precipitates. Additionally, we have performed a quantitative study of the morphology of two-dimensional multi-precipitate microstructures during growth and coarsening, and compared the calculated results with experimentally observed morphologies. Our multiscale first-principles/phase-field method is completely general and should therefore be applicable to a wide variety of problems in microstructural evolution.

1. Introduction

The solid-state Al-rich portion of the Al–Cu phase diagram consists of an Al solid solution and a two-phase field between the Al solid solution and θ-Al$_2$Cu, an ordered intermetallic phase. θ is the thermodynamically stable phase at high temperatures (for a discussion of the low-temperature stability, however, see [1]) but is kinetically unfavorable for direct precipitation from the solid solution, especially at temperatures below 250 °C. The kinetically driven precipitation reaction below 250 °C proceeds through a well accepted sequence of transformations:

$$\text{Al}_{SS}(\text{supersaturated}) \rightarrow \text{Al}_{SS} + \text{GP zones} \rightarrow \text{Al}_{SS} + \theta'$$
$$\rightarrow \text{Al}_{SS} + \theta,$$

where Al$_{SS}$ represents the aluminum solid solution, and the Guinier–Preston (GP) zones and θ' are metastable precipitate phases. Experimental measurements of mechanical properties as a function of aging time, aging temperature, and alloy composition show that the maximum hardness that occurs in the temperature range of 190–230 °C in binary Al–Cu alloys is associated with the presence of θ' precipitates in the alloy [2,3]. Mechanical properties, such as yield strength, are controlled not merely by the amount of θ' present, but also by the morphology of the θ' precipitate microstructure. Thus, understanding the morphology and evolution of precipitate microstructure is a key step towards predictive modeling of mechanical properties.

A large amount of experimental work has yielded a wealth of information about θ' crystal structure, morphology, and interface structure: θ'-Al$_2$Cu is a tetragonal phase (a slight tetragonal distortion of the cubic CaF$_2$ structure) with the the following orientation

---
* Corresponding author. Tel.: +1-814-865-0298; fax: +1-814-863-0618.
E-mail address: vxv115@psu.edu (V. Vaithyanathan).

relationship with the Al-matrix $(001)_{\theta'} \| \{001\}_{Al}$ [4]. This orientation relationship, where the c-axis of the tetragonal precipitate aligns along the cube axes of the fcc matrix, gives rise to three orientational variants. θ' precipitates possess a plate-shaped morphology with coherent $(001)_{\theta'} \| \{001\}_{Al}$ interfaces along the broad faces of the plates and semi-coherent interfaces around the rim of the plates [4–8]. The observed, large aspect ratios of θ' plates (often $\sim$40 and higher) vary with aging conditions and the processing history of the sample.

In the present work, we use a predictive, multiscale computational methodology to elucidate the physical factors controlling the θ' morphology in Al–Cu alloys. Despite the fact that the θ' precipitate/matrix interfaces are coherent along broad faces and semi-coherent around the rims of the plates, many theoretical analyses related to the equilibrium aspect ratios of θ' plates have only considered the interfacial energy anisotropy, i.e. the coherency strain energy contribution to morphology is ignored. A recent study, however, has analyzed the observed morphologies of θ' plates within the framework of Khachaturyan–Hairapetyan thermoelastic theory, including both interfacial and coherency strain effects [9]. These authors have found that this theory could successfully explain many of the observed morphologies. However, the Khachaturyan–Hairapetyan thermoelastic theory is formulated in terms of such quantities as the interfacial energies and elastic constants of precipitate and matrix, and many of these quantities are unknown for the θ'/Al case. Therefore, the authors in [9] inferred the unknown quantities from measured precipitate morphologies. We take a different approach. We wish to *calculate* all of the physical quantities controlling the θ' morphology starting from highly accurate first-principles total energy calculations. We then transfer the information from these atomic scale first-principles derived quantities to a mesoscale phase-field model of θ' microstructural evolution, and analyze the effects of the various physical contributions on precipitate morphology. We recently introduced this multiscale model in [10], and the present work provides a more detailed account of the various computational models involved as well as the links between them. Further, we test the quantitative predictions of the multiscale model via a critical comparison against measured data on θ' morphologies (diameter, thickness, aspect ratio) as a function of aging time. In addition, we use our model to elucidate the relevant physical factors controlling θ' morphology.

The crux of our multiscale model is the phase-field method, a powerful technique for modeling the microstructure evolution during phase transformations and coarsening ([11] and references therein). However, the phase-field method relies on various energy contributions that drive the microstructure evolution: (i) bulk, (ii) interfacial and (iii) coherency strain energies. The dearth of reliable values of these energetic parameters from experiments has been one primary reason for the predominantly qualitative nature of microstructure studies using phase-field. We show how first-principles calculations based on density functional theory (DFT) may be used to compute all of the energetic contributions entering the phase-field model. Thus, we arrive at a truly *predictive* model of microstructural evolution.

2. Methodologies used to construct the multiscale model

The multiscale model, which is an integration of many different computational methodologies, is illustrated in Fig. 1. We next briefly describe each of these methodologies.

2.1. First-principles total energies

First-principles calculations used in this work are based on density functional theory within the local density approximation (LDA) with the exchange-correlation of Ceperley and Alder [12,13]. In some cases, we have also compared the LDA results with those from generalized gradient approximation (GGA) of Perdew [14]. For total energy calculations, we use both full-potential linearized augmented plane wave method (FLAPW) [15] and the pseudopotential method utilizing ultrasoft pseudopotentials as implemented in the Vienna ab initio Simulation Package (VASP) [16]. The first-principles vibrational entropies used in this work are taken from the linear response calculations of Wolverton and Ozolins [1], which utilized norm-conserving pseudopotentials.

Using extensive tests, we have ensured that the first-principles energetics are converged with respect to k points (up to $16 \times 16 \times 16$ grids were used) and basis-set cutoffs ($E_{cut} = 16.7$ and 21.5 Ryd were used in the
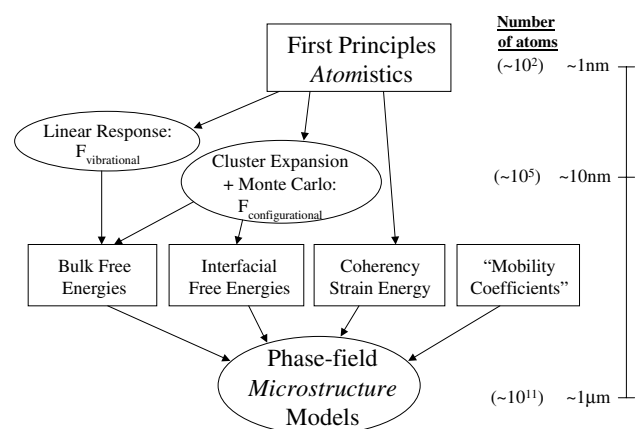

Fig. 1. Schematic of the multiscale model, showing different constituent models and their links along with their associated length scales.

Comparison of VASP vs. FLAPW Energetics:
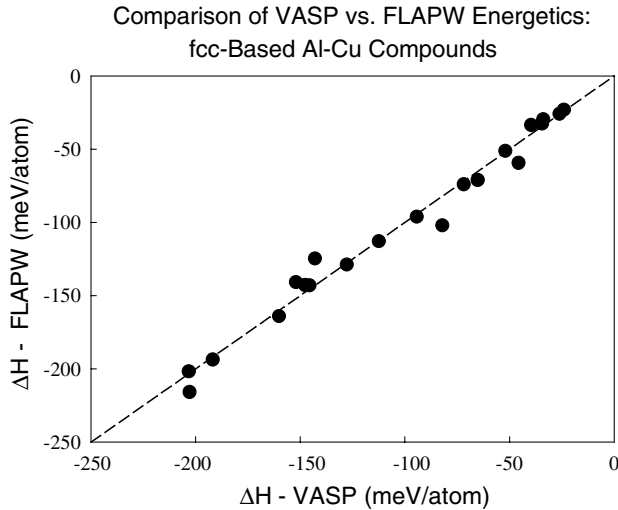fcc-Based Al-Cu Compounds

Fig. 2. Comparison of FLAPW and VASP formation energies of more than 20 different fcc-based fully relaxed ordered compounds of Al–Cu. The average deviation between the two methods' energies is extremely small (∼6 meV/atom out of the average formation energies of more than 100 meV/atom), thus inspiring confidence that the FLAPW/VASP energies are basically interchangeable for this system.

FLAPW and VASP calculations, respectively). The structures, in all cases, were fully relaxed with respect to volume as well as all cell-internal and -external coordinates. The combination of different first-principles energetics into a single microstructural model might initially cause concern, however, we tested the formation energies of more than 20 different fully relaxed fcc-based ordered compounds of Al–Cu with both the FLAPW and VASP methods. The average deviation between the two methods' energies is extremely small (∼6 meV/atom out of the average formation energies of more than 100 meV/atom), thus inspiring confidence that the FLAPW/VASP energies are basically interchangeable for this system. The comparison between FLAPW and VASP energies in Al–Cu is shown in Fig. 2.

2.2. Mixed-space cluster expansion

The calculation of finite temperature free energy of a disordered solid solution phase is outside the realm of *direct* first-principles calculations, due to the disorder involved as well as the configurational entropy contribution associated with it. However, the mixed-space cluster expansion (MSCE) technique parameterized from first-principles calculations enables the calculation of disordered solid solution phases at finite temperatures including the important energetic effects of atomic relaxations, all with the accuracy of first-principles energies [17]. In the MSCE technique, energetics of small unit cell ordered compounds are mapped onto a generalized Ising-like model for a particular lattice type, involving 2-, 3-, and 4-body interactions plus coherency

strain energies (atomic misfit strain). The Hamiltonian can be incorporated into mixed-space Monte Carlo simulations of $N \sim 10^5$ atoms [18], effectively allowing one to explore the complexity of the 2^N configurational space at finite temperatures. The mixed-space CE Hamiltonian for fcc Al–Cu used here has been previously constructed from first-principles total energies of 41 ordered structures [18].

2.3. Monte Carlo simulations and thermodynamic integration

Using the first-principles MSCE Hamiltonian in Monte Carlo simulations, we can obtain the energy (per atom) of the Al–Cu solid solution (E_{SS}) as a function of temperature for different solute (Cu) compositions. The mixing enthalpy of the solid solution (ΔH_{SS}) is obtained from E_{SS} by subtracting the composition-weighted average of the pure constituent energies

$$\Delta H_{SS} = E_{SS} - [X_{Cu}E_{Cu} + (1 - X_{Cu})E_{Al}], \qquad (1)$$

where X_{Cu} is the concentration of copper, and E_{Cu} and E_{Al} are the energies per atom of copper and aluminum, respectively, in their equilibrium fcc structures. Monte Carlo simulations can give energetics such as Eq. (1) directly as an output. However, the entropy cannot be directed computed in a Monte Carlo simulation; instead one must use techniques such as thermodynamic integration: The configurational entropy of the disordered alloy at any finite temperature T is computed from a Monte Carlo simulation starting at very high temperatures ("$T = \infty$") and slowly cooling down [19]. The following thermodynamic relation gives the configurational entropy at temperature T

$$\Delta S_{conf}(T) = \Delta S_{ideal} + \frac{\Delta H_{SS}(T)}{T} - k_B \int_0^\beta \Delta H_{SS}(\beta') \, d\beta', \qquad (2)$$

where $\Delta S_{ideal} = -k_B[X_{Cu} \ln(X_{Cu}) + (1 - X_{Cu}) \ln(1 - X_{Cu})]$ is the configurational entropy of an ideal solution (reference entropy at $T = \infty$), and $\beta = 1/(k_B T)$, where T is the temperature (in K) and k_B is the Boltzmann constant. The free energy is then given by

$$\Delta F_{SS}(T) = \Delta H_{SS}(T) - T\Delta S_{conf}(T)$$
$$= \frac{1}{\beta} \int_0^\beta \Delta H_{SS}(\beta') \, d\beta' - T\Delta S_{ideal}. \qquad (3)$$

To facilitate the integration in Eq. (3), we fit the mixing enthalpy to a polynomial in β.

The vibrational entropy contribution to the solid solution free energy is not included in this calculation. While a systematic computation of the vibrational entropy of configurationally disordered solid solutions in Al–Cu would be interesting, the complexity of such calculations is considerable.

2.4. Phase-field model

In the phase-field methodology, a precipitate microstructure is described by a set of continuum order parameter fields characterizing the difference in composition and structure between the precipitate and matrix [11]. In a two-dimensional representation of θ' precipitates in a binary Al–Cu alloy, the precipitate microstructure is described by one composition field and two orientation-related long range order parameter fields.

The chemical free energy of the microstructure, including the bulk and interfacial energy, is then expressed as

$$F_{\text{bulk}} + F_{\text{int}} = \int_V \left(f(c, \eta_1, \eta_2, \eta_3) + \frac{\alpha}{2}(\nabla c)^2 \right. \\ \left. + \frac{1}{2} \sum_p \beta_{ij}(p)\nabla_i \eta_p \nabla_j \eta_p \right) dV, \tag{4}$$

where α and $\beta_{ij}(p)$ are gradient energy coefficients for composition and order parameters, respectively. $\beta_{ij}(p)$ is retained as a second rank tensor to incorporate the (tetragonal) anisotropy in interfacial energy. The anisotropy in interfacial energy of the precipitate is dependent on the orientational variant, η, of the precipitate (see Fig. 3). Since the phase-field model used in this study is a dislocation-free model, semi-coherent interfaces are treated effectively as coherent interfaces with a larger interfacial energy.

$$\beta_{ij}(1) = \begin{pmatrix} \beta_{11}(1) & 0 \\ 0 & \beta_{22}(1) \end{pmatrix},$$
$$\beta_{ij}(2) = \begin{pmatrix} \beta_{11}(2) & 0 \\ 0 & \beta_{22}(2) \end{pmatrix} = \begin{pmatrix} \beta_{22}(1) & 0 \\ 0 & \beta_{11}(1) \end{pmatrix}. \tag{5}$$
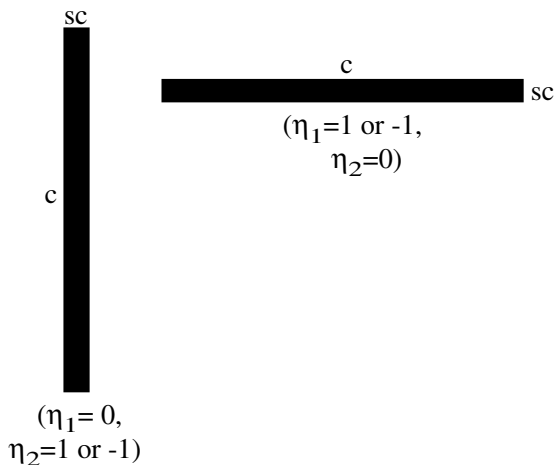

Fig. 3. Schematic of the θ' precipitates in 2D showing the two variants along with their equilibrium order parameters. The interfaces of the variants are marked as coherent (c) and semi-coherent (sc) to show the symmetry and the interface orientation dependence on the variants.

The bulk free energy describing the phase-separation and order-disorder transformation involved during precipitation of the θ' phase is approximated using the following polynomial in c and η:

$$f(c, \eta_1, \eta_2, \eta_3) \\ = A_1(c - C_1)^2 + A_2(c - C_2)(\eta_1^2 + \eta_2^2 + \eta_3^2) \\ + A_{41}(\eta_1^4 + \eta_2^4 + \eta_3^4) + A_{42}(\eta_1^2\eta_2^2 + \eta_2^2\eta_3^2 + \eta_1^2\eta_3^2) \\ + A_{61}(\eta_1^6 + \eta_2^6 + \eta_3^6) \\ + A_{62}\{\eta_1^4(\eta_2^2 + \eta_3^2) + \eta_2^4(\eta_3^2 + \eta_1^2) + \eta_3^4(\eta_1^2 + \eta_2^2)\} \\ + A_{63}(\eta_1^2\eta_2^2\eta_3^2), \tag{6}$$

where C_1 and C_2 are constants close to the equilibrium compositions of solid solution matrix and θ' precipitates, respectively. The coefficients A_{41} and A_{61} are constrained to have negative and positive values, respectively, to describe a first order phase transition [20].

The elastic energy contribution to the total free energy of the system is obtained analytically using the method of Khachaturyan [21,22]. The stress-free misfit strain, $\epsilon_{ij}^0(\mathbf{r})$, between precipitates and matrix, is expressed as a function of the structural order parameters,

$$\epsilon_{ij}^0(\mathbf{r}) = \sum_p \epsilon_{ij}^0(p)\eta_p^2(\mathbf{r}), \tag{7}$$

where $\epsilon_{ij}^0(p)$ represents the stress-free strain of the pth variant. With the homogeneous modulus approximation (matrix and precipitates have similar elastic constants), the elastic energy in terms of order parameters can be expressed as [23]

$$E_{\text{el}} = \frac{V}{2}\lambda_{ijkl}\bar{\epsilon}_{ij}\bar{\epsilon}_{kl} - V\lambda_{ijkl}\bar{\epsilon}_{ij}\sum_p \epsilon_{kl}^0(p)\overline{\eta_p^2(\mathbf{r})} \\ + \frac{V}{2}\lambda_{ijkl}\sum_p \sum_q \epsilon_{ij}^0(p)\epsilon_{kl}^0(q)\overline{\eta_p^2(\mathbf{r})\eta_q^2(\mathbf{r})} \\ - \frac{1}{2}\sum_p \sum_q \int \frac{d^3\mathbf{g}}{(2\pi)^3}B_{pq}(\mathbf{n})\{\eta_p^2(\mathbf{r})\}_{\mathbf{g}}^*\{\eta_q^2(\mathbf{r})\}_{\mathbf{g}}, \tag{8}$$

where λ_{ijkl} is the elastic stiffness tensor. $B_{pq}(\mathbf{n}) = n_i\sigma_{ij}(p)\Omega_{jk}(\mathbf{n})\sigma_{kl}(q)n_l$ and $\Omega_{jk}(\mathbf{n})$ is the inverse matrix of $\Omega_{jk}^{-1}(\mathbf{n}) = n_i\lambda_{ijkl}n_l$. $\mathbf{n} = \mathbf{g}/|\mathbf{g}|$ is the unit vector in reciprocal space, $\{\eta_q^2(\mathbf{r})\}_{\mathbf{g}}$ is the Fourier transform of the square of order parameter $[\eta_q^2(\mathbf{r})]$ and $\{\eta_p^2(\mathbf{r})\}_{\mathbf{g}}^*$ is the complex conjugate of $\{\eta_p^2(\mathbf{r})\}_{\mathbf{g}}$. $\bar{\epsilon}_{ij} = \bar{\epsilon}_{ij}^0 + \bar{\epsilon}_{ij}^a$ is the sum of homogeneous strain caused by transformation and external constraints or applied stress, respectively. In the absence of applied strain, the fourth term in the elastic energy (Eq. (8)) is the dominant term controlling the precipitate morphology.

The temporal evolution of the microstructure in the phase-field model is obtained by numerically solving the Cahn–Hilliard and Allen–Cahn equations [24]

$$\frac{\partial c(\mathbf{r}, t)}{\partial t} = M\nabla^2 \frac{\delta F}{\delta c(\mathbf{r}, t)}, \tag{9}$$

$$\frac{\partial \eta_i(\mathbf{r}, t)}{\partial t} = -L(\hat{\phi}_p)\frac{\delta F}{\delta \eta_i(\mathbf{r}, t)}, \quad i = 1, 2, 3, \tag{10}$$

where M is the solute mobility and $L(\hat{\phi}_p) = LA(\hat{\phi}_p)$ is the orientation-dependent interfacial kinetic parameter. L is the interfacial kinetic coefficient. Interface orientation is defined by the unit normal to the precipitate interface, $\hat{\phi}_p$ ($= \vec{\nabla}\eta_p/|\vec{\nabla}\eta_p|$). The anisotropy in interfacial kinetics can be incorporated as a function of the interface normal ($\hat{\phi}_p$).

The temporal equations (Eqs. (9) and (10)) in dimensionless form can be reduced to

$$\frac{\partial c}{\partial t^*} = M^*\nabla^2\left[\frac{\partial f^*}{\partial c} - \xi\nabla^2 c\right], \tag{11}$$

$$\frac{\partial \eta_p}{\partial t^*} = -\frac{L(\hat{\phi}_p)}{L}\left[\frac{\partial f^*}{\partial \eta_p} - \psi_{ii}(p)\nabla_i^2\eta_p + \frac{\delta E_{el}^*}{\delta \eta_p}\right], \tag{12}$$

$$t^* = L|\Delta f|t, \quad r^* = r/l, \tag{13}$$

$$M^* = \frac{M}{Ll^2}, \quad f^* = \frac{f(c, \eta)}{|\Delta f|}, \quad E_{el}^* = \frac{E_{el}}{|\Delta f|},$$

$$\xi = \frac{\alpha}{|\Delta f|l^2}, \quad \psi_{ii}(p) = \frac{\beta_{ii}(p)}{|\Delta f|l^2}, \tag{14}$$

where the quantities with asterisk (*) represent the dimensionless equivalent of the corresponding dimensional values. l represents the grid spacing (Δx) or the characteristic length scale and Δf represents the characteristic free energy (usually the maximum driving force for phase transformation from the constructed bulk free energy). The temporal equations are solved numerically using the semi-implicit Fourier-Spectral method [25].

3. Results: first-principles calculations

3.1. Bulk chemical free energy

3.1.1. Solid solution phase

The enthalpy and free energy (in meV/atom) as a function of composition and temperature, obtained from the combined first-principles/MSCE/Monte Carlo approach, are shown in Figs. 4(a) and (b), respectively. We note that the temperature dependence of enthalpy in Fig. 4(a) is due to a clustering-type short range order (SRO) in the Monte Carlo simulations of the Al–Cu alloy. For a more detailed discussion of the predicted and experimentally measured SRO in Al–Cu, see [26]. We also note that our calculated free energy for the solid solution phase includes configurational but not vibrational entropic contributions.

3.1.2. θ' precipitate phase

The MSCE Hamiltonian obtained for the solid solution free energy calculations based on first-principles
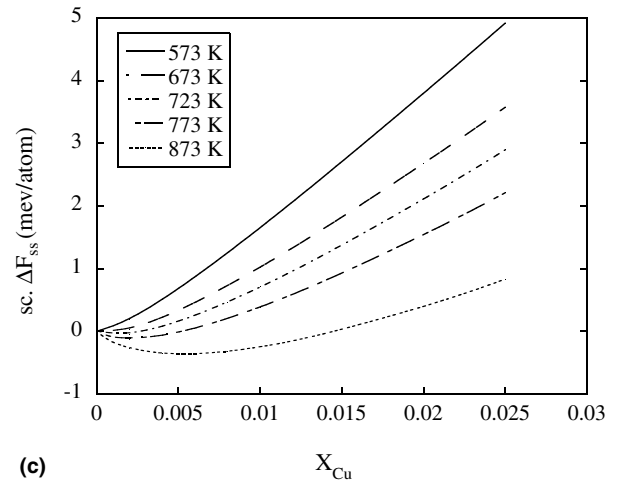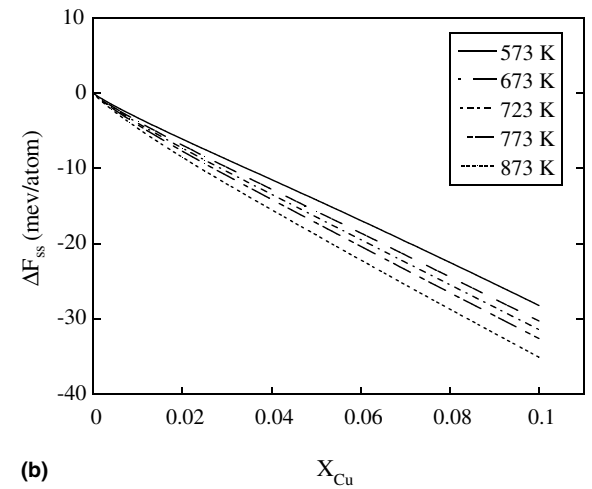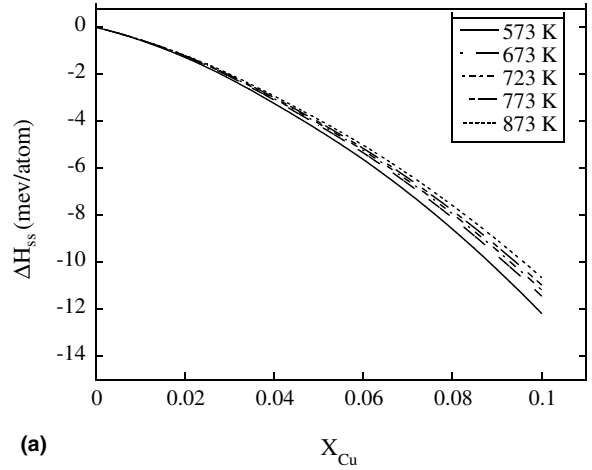

Fig. 4. (a) Enthalpy, (b) free energy and (c) scaled free energy of the Al–Cu solid solution as a function of solute composition and temperature, calculated using the first-principles (FLAPW-LDA) MSCE combined with thermodynamic integration. The scaled free energy is obtained by adding a linear term in composition $[-3X_{Cu}\ \Delta F_{\theta'}(T)]$, such that the rescaled θ' free energy at $X_{Cu} = 1/3$ is zero. This linear scaling of the free energy does not affect the determination of equilibrium composition through the common tangent construction, but merely aids in visualization.

energetics is applicable only for substitutional fcc-based configurations. It can be used for calculating the free energy of an fcc-based compound (e.g., a structure that can be represented by a substitutional decoration of A and B atoms on the sites of an fcc lattice, such as an ordered $L1_2$ or $L1_0$), but cannot be used for calculating the free energy of θ', which has a (distorted) CaF_2 crystal structure. Hence, the θ' energy is obtained from direct first-principles calculations at $T = 0$ K, coupled with the vibrational entropy of θ', which has been found to be unexpectedly important for this phase [1]. Additionally, by performing point defect calculations of supercells of θ' and inserting the energetics into a low-temperature expansion, we find that the configurational entropy of θ' is small, and we do not consider θ' off-stoichiometry. The θ' formation enthalpy was calculated from first-principles as −195.8 meV/atom at Al_2Cu stoichiometry ($X_{Cu} = 1/3$). The computed (formation) vibrational entropy is $-0.62k_B$ [1]. Hence, the free energy of θ' as a function of temperature is given by

$$\Delta F_{\theta'}(T) = -195.8 + 0.62k_BT \quad (\text{in meV/atom}). \qquad (15)$$

We note that without the inclusion of the θ' vibrational entropy term, the calculated equilibrium solubility of Cu in solid solution is extremely small. For easier visualization, the free energy is scaled by a linear term in composition $[-3X_{Cu} \, \Delta F_{\theta'}(T)]$, such that the rescaled θ' free energy at $X_{Cu} = 1/3$ is zero (Fig. 4(c)). This linear scaling of the free energy does not affect the determination of equilibrium composition through the common tangent construction.

3.2. Interfacial energy

In a system where the precipitate and matrix phases are substitutional rearrangements of atoms on the same lattice type, and form perfectly coherent interfaces (e.g., GP zone phases), one could calculate the interfacial free energy from a Monte Carlo simulation coupled with thermodynamic integration, analogous to the procedure described for bulk free energies. Alternatively, $T = 0$ K values may be obtained from direct first-principles supercell calculations (without using a CE). θ' precipitates are partially coherent with different crystal structures for precipitate and matrix. Hence, it is not amenable to the CE method. Therefore, we extract the $T = 0$ K interfacial energies directly from first-principles supercell calculations. We next describe how the interfacial energies are extracted from supercell energetics, and separated from the coherency strain energetics.

We begin by considering an N-atom coherent supercell containing an interface between two materials, A and B (in the case of this work, $A = $ Al and $B = Al_2Cu$ θ'). For simplicity, we consider the case of cells comprising equal amount of A and B. The energy of a such an $A_{N/2}B_{N/2}$ supercell can be separated into two com-

ponents [27]: (a) *coherency strain* (cs): the strain energy required to maintain coherency between the (lattice mismatched) materials A and B, and (b) *interfacial energy*: the energy associated with the interactions between materials at the A/B interface(s). To define these terms, it is useful to first consider the infinite period supercell limit $N \rightarrow \infty$, for a supercell with interface along an orientation $\hat{G}$ with lattice constants $a_\parallel$ and $a_\perp$ parallel and perpendicular to $\hat{G}$, respectively. In this infinite-period case, A/B interfacial interactions (which scale as the *area* of the interface) contribute a negligible amount to the supercell formation energy δE_{sup} (which scales as the *volume* of the superlattice):

$$\delta E_{\text{sup}}(N \rightarrow \infty, \hat{G})$$
$$\equiv \delta E_{CS}(\hat{G}) = \min_{a_\perp} \left[\frac{1}{2}\delta E_A^{\text{epi}}(a_\perp, a_\parallel^A, \hat{G}) + \frac{1}{2}\delta E_B^{\text{epi}}(a_\perp, a_\parallel^B, \hat{G}) \right], \qquad (16)$$

where δE_{sup} is the energy of the supercell relative to equivalent amounts of A and B in their equilibrium bulk geometries. In Eq. (16), the materials A and B are deformed in an "epitaxial" geometry: Both materials are brought to a common lattice constant $a_\perp$ perpendicular to $\hat{G}$, and the energy of each material is individually minimized with respect to the lattice constant $a_\parallel$ parallel to $\hat{G}$. The epitaxial energies δE_{epi} are the energies of A and B in these epitaxial geometries relative to their equilibrium bulk energy. For finite-period supercells, the energy is determined not only by the coherency stain energy, but also by the interfacial energy σ times the number (2) and area (A) of these interfaces. Since we are using energetics per atom, we must divide by the number of atoms in the cell, N. The interfacial energy is then defined as

$$\delta E_{\text{sup}}(N, \hat{G}) - \delta E_{\text{sup}}(N \rightarrow \infty, \hat{G}) \equiv \frac{2\sigma(\hat{G})A}{N}. \qquad (17)$$

Combining Eqs. (16) and (17), we see the decomposition of the supercell energy (for *any* period) into strain and interfacial components

$$\delta E_{SL}(N, \hat{G}) = \frac{2\sigma(\hat{G})A}{N} + \delta E_{CS}(\hat{G}). \qquad (18)$$

From Eq. (18), we see that if the supercell formation energies (per atom) are plotted as a function of $1/N$, the slope is just $2\sigma A$, and the y-intercept is $\delta E_{CS}(\hat{G})$. We have extracted the interfacial energies from first-principles supercell calculations using the construction of Eq. (18). The results are shown in Fig. 6. We note that extracting the coherency strain energy from these calculations is not numerically stable; a more robust approach is the direct calculation of Eq. (16) described below.

The tetragonal structure of θ' precipitate embedded in an fcc matrix results in partially coherent plate-shaped precipitates. The θ' plates possess a broad coherent face
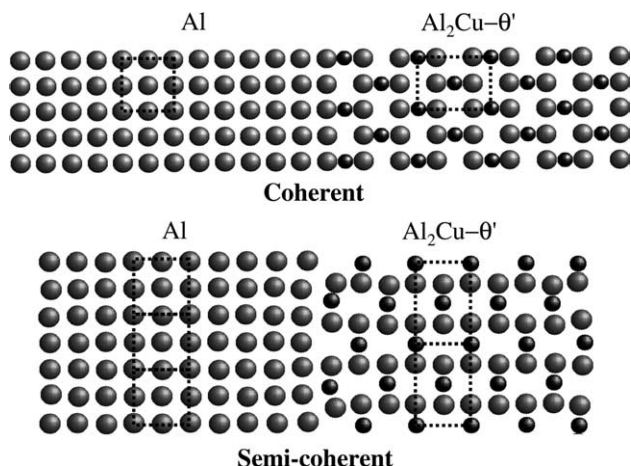
Fig. 5. Relaxed supercells from the first-principles interfacial energy calculations of coherent $(1\,0\,0)$ and semi-coherent $(0\,0\,1)$ interfaces of θ'-Al$_2$Cu in fcc Al solid solution [10]. Dashed lines indicate the $1a_{\theta'} = 1a_{Al}$ and $2c_{\theta'} = 3a_{Al}$ relationships of the coherent and semi-coherent interfaces, respectively.

Fig. 6. First-principles (VASP) formation energies of Al/θ' N-atom supercells as a function of $1/N$ for both interfaces shown in Fig. 5. Energetics are shown for both LDA (filled symbols) and GGA (empty symbols) calculations. The energies of the large-cell calculations are fit to straight lines, and the interfacial energies (σ) are extracted from the slopes, $2\sigma A$, of these lines [see Eq. (18)].

and a semi-coherent rim. We construct supercells consistent with the observed orientation relations between θ' and the Al matrix: $(0\,0\,1)_{\theta'} \| \{0\,0\,1\}_{Al}$ and $[0\,1\,0]_{\theta'} \| [0\,1\,0]_{Al}$ [4]. Representative cells showing the interfacial structures are given in Fig. 5. Although the present phase-field model is 2D, we note that the first-principles calculations used to generate the various energetics of the θ'/Al system are fully three-dimensional. The coherent and semi-coherent interfaces possess very different interfacial structures. Due to lattice-misfit arguments (see below), the semi-coherent interface structure is found to have a 2 θ' to 3 Al$_{SS}$ unit cell arrangement. This configuration was proposed by Stobbs and Purdy [8] and confirmed by their TEM strain field observations around the interface.

From Fig. 6, we see that the calculated $T = 0$ K interfacial energies from first-principles LDA calculations of the coherent and semi-coherent interfaces are 190 and 600 mJ/m^2, respectively. GGA calculations, give slightly lower values of 170 and 520 mJ/m^2, respectively. (The LDA numbers given here are slightly smaller than previous values published in [10] due to a more careful consideration of **k**-point convergence.) From our convergence studies, we estimate an uncertainty in these calculated interfacial energies on the order of 5–10% due to supercell size. Interestingly, for both LDA and GGA, the interfacial anisotropy between semi-coherent and coherent interfaces is consistently around 3. In addition to the isolated interface energies, one can obtain some indication of the interface-interface interactions from the energies in Fig. 6 for relatively small supercells. For the coherent interface, the small-cell energies fall above the line extracted from large cells, thus indicating a repulsion between these interfaces at short distances. For
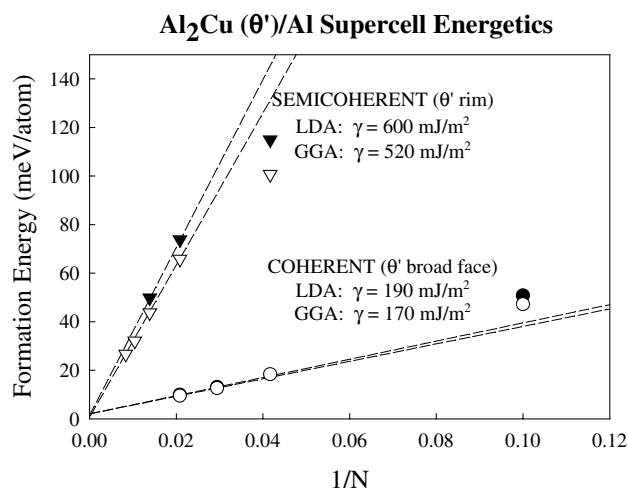
the semi-coherent interface, the opposite is true, i.e., these interfaces tend to attract one another at short separations.

We can contrast our first-principles calculated interfacial anisotropy of ~3 with a previous estimate by Aaronson and Laird [28] of ~12. Our first-principles calculations include more physical contributions, and hence, are more predictive and certainly more accurate than the previous highly simplified estimate [28]. Therefore, we assert that the currently most reliable value of the interfacial anisotropy for the θ'/Al system is ~3. This is noteworthy, since the anisotropy estimate of 12 has been widely used in the literature as a prediction of the *equilibrium aspect ratio* of θ'. These estimates of the equilibrium aspect ratio are flawed not only because we have shown the more accurate interfacial anisotropy is ~3, but also there exists a strong strain anisotropy contribution in this system (discussed in the next section), which can significantly alter the equilibrium aspect ratio of θ' precipitates.

We note that the interfacial energy anisotropy obtained from first-principles is obtained at $T = 0$ K and for a completely sharp interface (Fig. 5). It would be of considerable interest to know how this anisotropy changes with temperature. At finite temperature, the interfaces will naturally be diffuse to some extent and hence, configurational degrees of freedom will alter the individual interfacial energy values. Also the vibrational entropy at the interface should be considered in a complete description of the temperature-dependence of the interfacial free energies. Future work along these lines would be most interesting.

3.3. Elastic properties

In addition to bulk and interfacial energies, there is a significant elastic energetic contribution to the θ'/Al system, due to the fact that the θ' precipitates are coherently strained by the Al matrix. The θ' plates are generally acknowledged to be coherent with the matrix along their broad faces. In addition, Doherty [7] has shown that the interfacial rim of plate-shaped precipitates are not necessarily incoherent, but could also be coherent or semi-coherent. Observations of the presence of facets on the rims of θ' precipitates (when viewed perpendicular to the coherent face of the plate) from TEM micrographs [4,29] prove that this interface is not completely incoherent. Thus, equilibrium morphology calculations, such as in the present work, should include the contributions from the elastic energy anisotropy in addition to the interfacial energy anisotropy.

To include the elastic energy contribution in the phase-field model, we require the following: the stress-free misfit strains along the coherent and semi-coherent interfaces and the resulting elastic strain energy contributions from the coherency constraints. These quantities are all readily calculated from our first-principles methods.

3.3.1. Stress-free misfit strains

The equilibrium or stress-free $T = 0$ K lattice parameters of pure, bulk fcc Al and θ'-Al$_2$Cu (CaF$_2$ structure) calculated using first-principles (FLAPW-LDA) are

$$a_{\text{Al}} = 0.3989 \text{ nm}, \quad a_{\theta'} = 0.4016 \text{ nm},$$

$$c_{\theta'} = \sqrt{2}a_{\theta'} = 0.5679 \text{ nm}.$$

We note that very large $\mathbf{k}$-point sets have been used to ensure the convergence of these structural parameters to several significant digits. From these lattice parameters, the calculated misfit δ_c along the coherent, *broad face* of θ' plates is

$$\delta_c = \frac{a_{\theta'} - a_{\text{Al}}}{a_{\text{Al}}} = +0.7\%. \tag{19}$$

Although the θ' plates are completely coherent across the broad face for lower aging temperatures, they may contain widely spaced misfit dislocations at higher aging temperatures [30]. By measuring the dislocation spacing across θ' broad faces, Weatherly and Nicholson [30] have inferred a misfit value of $|\delta_c| = 0.57\%$, which agrees well with our first-principles calculated misfit. We also note that Weatherly and Nicholson could not ascertain the *sign* of the misfit from their observations, as they could not unambiguously determine the nature of the Burgers vectors of the dislocations; our calculations clearly show that the θ' plates are under a compressive strain along the broad faces.

Around the *precipitate rim*, the simple configuration of $c_{\theta'} : a_{\text{Al}}$ has an extremely large misfit strain of 42%.

Therefore, we have considered the misfit for a few integer combinations of $c_{\theta'}$ and a_{Al} unit cells. For a configuration of $\mathbf{m}$ θ' to $\mathbf{n}$ Al unit cells, respectively, where $\mathbf{m}$ and $\mathbf{n}$ are positive integers, the misfit along the semi-coherent interface (δ_{sc}) defined as

$$\delta_{\text{sc}} = \frac{\mathbf{m}(c_{\theta'}) - \mathbf{n}(a_{\text{Al}})}{\mathbf{n}(a_{\text{Al}})} \tag{20}$$

is as follows for $\mathbf{m} \leqslant 4$: (i) $1c_{\theta'} : 1a_{\text{Al}}$ – +42.4%, (ii) $1c_{\theta'} : 2a_{\text{Al}}$ – −28.8%, (iii) $2c_{\theta'} : 3a_{\text{Al}}$ – −5.1%, (iv) $3c_{\theta'} : 4a_{\text{Al}}$ – +6.8%, (v) $3c_{\theta'} : 5a_{\text{Al}}$ – −14.6%, and (vi) $4c_{\theta'} : 5a_{\text{Al}}$ – +13.9%.

We verify that the $2c_{\theta'} : 3a_{\text{Al}}$ configuration for the semi-coherent interface, observed by Stobbs and Purdy [8], is the most favorable low-integer combination in terms of lattice misfit with $\delta_{\text{sc}} = -5.1\%$. Lattice parameter measurements of θ' give a value of $\delta_{\text{sc}} = -4.3\%$ for this misfit [8,31]. Again, our calculations are in reasonable agreement with observations. We note that for larger-unit cell combinations (i.e., thicker θ' plates), one can obtain even smaller misfit strains: For example, the $5c_{\theta'} : 7a_{\text{Al}}$ and $7c_{\theta'} : 10a_{\text{Al}}$ combinations have $\delta_{\text{sc}} = +1.7\%$ and -0.3%, respectively. However, we confine our attention in this work to the $2c_{\theta'} : 3a_{\text{Al}}$ configuration. For a more complete discussion of the interfacial structure, and mechanisms for θ' precipiate growth, we refer the reader to [4,8,31] and references therein.

3.3.2. Coherency strain energies:

For the phase-field model, we also need to know the strain energy penalty associated with the misfit strains calculated above. We have calculated the coherency strain energy for a θ'/Al system in an analogous manner to that used to construct the Al/Cu coherency strain entering the mixed-space cluster expansion [17,19]. This calculation involves a direct computation of Eq. (16) whereby Al and θ'-Al$_2$Cu are each deformed in an "epitaxial" geometry, strained to a common lattice constant in a plane perpendicular to an orientation, $\hat{G}$. Summing together these "epitaxial" energies and subsequently minimizing with respect to the common lattice constant gives the coherency strain energy of Eq. (16). Fig. 7 shows the calculated coherency strain for the θ'/Al system for hydrostatic strain, as well as epitaxial strain along [1 0 0] and [1 1 1] orientations.

We note that due to the homogeneous modulus approximation used in the phase-field model, it is necessary that we extract a single, averaged set of harmonic elastic constants from these calculations. We note that first-principles total energy calculations are not constrained by the homogeneous modulus approximation, nor by harmonic elasticity theory, and include both harmonic and anharmonic elastic effects. However, we analyze our results within the context of harmonic elasticity, and use this theory to extract the average elastic modulii of the θ'/Al system from the results of
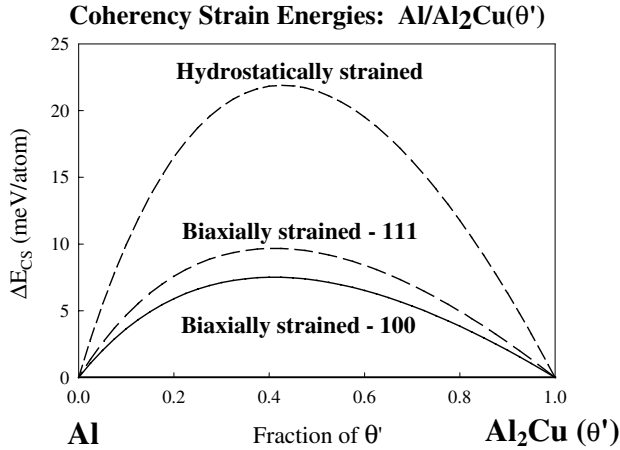
Coherency Strain Energies: Al/Al₂Cu(θ')

Fig. 7. First-principles (FLAPW-LDA) coherency strain energies of the Al/θ' system. Shown are strain energies for hydrostatic deformation, as well as epitaxial deformation along [1 0 0] and [1 1 1] orientations. The strain energies shown are for the coherency constraint of the semi-coherent interfaces (around the rims of the plates), $2c_{\theta'} : 3a_{Al}$. The strain energies for the broad face coherency constraint, $a_{\theta'} : a_{Al}$ (not shown), are qualitatively similar, but substantially reduced in magnitude due to the smaller misfit in this orientation.

Fig. 7. The epitaxial softening function [19] is given by the ratio of the epitaxial strain energy along an orientation $\hat{G}$ and the strain energy for hydrostatic deformation, each deformed to a lattice parameter a_S:

$$q(\hat{G}, a_S) = \frac{\delta E^{epi}(\hat{G}, a_S)}{\delta E^{hydro}(a_S)}. \tag{21}$$

In harmonic elasticity theory, this softening function is given by

$$q_{harm}(\hat{G}) = 1 - \frac{B}{C_{11} + \Delta\gamma_{harm}}, \tag{22}$$

where B is the bulk modulus, C_{ij} are the elastic constants, $\Delta = C_{44} - \frac{1}{2}(C_{11} - C_{12})$ is the elastic anisotropy parameter, and γ_{harm} is a geometric function of the spherical angles formed by $\hat{G}$ [19]. Specifically, for the principle high-symmetry directions,

$$\gamma_{harm}([0\,0\,1]) = 0, \quad \gamma_{harm}([1\,1\,0]) = 1, \quad \gamma_{harm}([0\,0\,1]) = 4/3. \tag{23}$$

From Fig. 7, we extract the values of $q([1\,1\,1])$ and $q([0\,0\,1])$ for a 5% phase fraction of θ'. Using these values and Eq. (22), we extract average modulii of $C_{12}/C_{11} = 0.442$ and $C_{44}/C_{11} = 0.428$. We note that these averaged modulii therefore contain information about the energetic penalty required to strain both the θ' precipitates and the Al matrix.

From the epitaxial deformation calculations described above, we have also extracted elastic constants of the cubic (CaF₂) θ' phase, as these constants are not available experimentally: $C_{11} = 1.9$ Mbar, $C_{12} = 0.8$ Mbar and $C_{44} = 0.9$ Mbar. The elastic anisotropy

$\Delta = +0.35$ Mbar > 0 indicates that θ' precipitate has an elastically soft direction along ⟨1 0 0⟩, as can also be seen from the results of Fig. 7.

4. Constructing the phase-field model

We have described how all the energetic inputs required for the phase-field microstructure modeling of Al-θ' system have been obtained from first-principles atomistic calculations. Next, we describe how the phase-field model is assembled from these energetics.

4.1. Coarse-grained free energy

The solid solution free energy from first-principles can be directly related to the first term in the coarse-grained free energy in the phase field model (Eq. (6)), i.e.

$$f(c, \eta_1 = 0, \eta_2 = 0, \eta_3 = 0) = A_1(c - C_1)^2. \tag{24}$$

The free energy of of the θ' phase in the phase-field model is given by $f(c, \eta_{eq}(c))$, where the equilibrium order parameter as a function of composition [$\eta_{eq}(c)$] is obtained by minimizing the bulk free energy

$$\eta_{eq}(c) = \pm\sqrt{\frac{-A_{41} \pm \sqrt{A_{41}^2 - 4A_{61}A_2(c - C_2)}}{2A_{61}}}. \tag{25}$$

The coefficients A_2, A_{41} and A_{61} are obtained using the first-principles calculated equilibrium free energy and equilibrium composition of θ'. The resulting coefficients (in meV/atom) of the coarse-grained free energy at 723 K in Eq. (6) from the fit are as follows:

$A_1 = 1622.6, \quad A_2 = 1075.1, \quad A_{41} = -536.6,$
$A_{61} = 536.6, \quad C_1 = 0.002, \quad C_2 = 0.3333.$

The coarse-grained free energy curves in Fig. 8 represent the two-phase equilibrium of Al solid solution and θ', described in the multiscale model based on coefficients obtained from first-principles. The maximum driving force for the transformation (at 723 K) from Fig. 8 is ~34 meV/atom, while the equilibrium compositions based on common tangent construction to the free energy curves are $c_\alpha = 0.0013$ (α represents the Al solid solution) and $c_{\theta'} = 0.3322$. The θ' free energy in Fig. 8 is admittedly an approximation to the first-principles calculated line compound free energy, introduced to avoid numerical instabilities. However, the approximated free energy reflects the proper equilibrium compositions of the two phases.

4.2. Gradient energy coefficients / interfacial energies

In the phase-field description, the interfacial energy 'σ' for a system described by both the composition and an order parameter is given by [32]
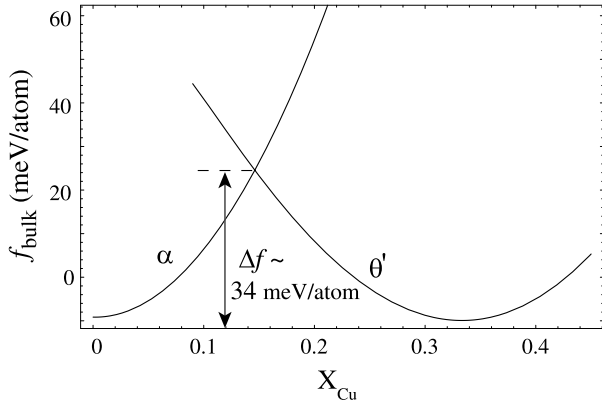
Fig. 8. Coarse-grained free energies of the matrix (α) and precipitates (θ') based on a polynomial fit to the energetics obtained by first-principles calculations at 723 K. Although θ' was determined to be a line compound from first-principles calculations, it is approximated by a polynomial with a smooth compositional dependence to avoid numerical instabilities.

$$\sigma = 2 \int_{c_\alpha}^{c_\beta} [\alpha \, \Delta f(c)]^{\frac{1}{2}} \left[1 + \sum_p \frac{\beta_{ij}(p)}{\alpha} \left(\frac{\mathrm{d}\eta_p}{\mathrm{d}c} \right)^2 \right]^{\frac{1}{2}} \mathrm{d}c, \quad (26)$$

where $\Delta f(c) = f(c) - f_{eq}(c)$ represents the excess free energy associated with the material in the interface, and α and $\beta_{ij}(p)$ represent the gradient energy coefficients of composition and order parameters (p-variants), respectively. Using the free energy described in Fig. 8 at 723 K and the first-principles calculated interfacial energy of Fig. 6, along with Eq. (26), we have obtained the gradient coefficients

$$\alpha = 6.13 \times 10^{-10}, \quad \beta_{11}(1) = 3.75 \times 10^{-10},$$

$$\beta_{22}(1) = 1.77 \times 10^{-9} \text{ (in J/m)}.$$

The coefficient α, which is the composition contribution to interfacial energy is fixed arbitrarily, in order to evaluate the coefficients β_{ij}. The calculated gradient energy values correspond to the first-principles calculated interfacial energy values of ~200 and ~600 mJ/m² for coherent and semi-coherent interfaces, respectively. The tetragonal symmetry of the variants are reflected in the $\beta_{ij}(1)$ values and the gradient coefficients for the second θ' variant [$\beta_{ij}(2)$] are obtained from Eq. (5).

4.3. Elastic contributions

The elastic energy expression in Eq. (8) requires the stiffness tensor (λ_{ijkl}) and stress-free strain tensor (ϵ_{ij}^0) as inputs, and we have demonstrated above how to obtain these quantities from first-principles. For cubic symmetry, C_{11}, C_{12} and C_{44} are the only independent coefficients in the matrix equivalent (C_{ij}) of the stiffness tensor (λ_{ijkl}). The strain tensor reflects the tetragonal symmetry in strain via the difference in misfit strain of the semi-coherent and coherent interfaces for the two precipitate variants

$$\epsilon_{ij}^0(1) = \begin{pmatrix} \epsilon_{11}(1) & 0 \\ 0 & \epsilon_{22}(1) \end{pmatrix} = \begin{pmatrix} \delta_{sc} & 0 \\ 0 & \delta_c \end{pmatrix},$$

$$\epsilon_{ij}^0(2) = \begin{pmatrix} \epsilon_{11}(2) & 0 \\ 0 & \epsilon_{22}(2) \end{pmatrix} = \begin{pmatrix} \delta_c & 0 \\ 0 & \delta_{sc} \end{pmatrix}, \quad (27)$$

where δ_c and δ_{sc} are the misfit strains along the coherent and semi-coherent interfaces, respectively. The orientational variants ($p = 1, 2$) in the strain tensor are arranged to be consistent with the gradient energy coefficient tensor (Eq. (5)) representing the interfacial energy anisotropy.

Based on the bulk free energy (coarse-grained Landau polynomial) constructed from first-principles data, and the first-principles calculated interfacial energy, we estimate the interfacial width of the coherent interface [$\sigma_{cal}/|\Delta f|$] to be ~1.2 nm. The grid spacing (Δx) is chosen to be 0.5 nm. We discuss below the implications of this choice of grid spacing. While the simulation can be easily extended to 3D, the present study is restricted to 2D because of the computational limitations involved in modeling a realistic system size in 3D. In 2D, the plate-shaped θ' precipitates will be modeled as if viewed edge-on and the number of orientational variants will be 2, instead of 3 (as in the schematic shown in Fig. 3). The 2D simulation grids were ~500×500–750×750 nm² depending on the volume fraction, the size restricted mainly by the availability of computational resources.

The phase-field model was constructed from first-principles data at ~450 °C. However, the exclusion of the vibrational entropy contribution in free energy calculations has been shown to cause an overestimation of the solvus temperature in Al–Sc alloys [33], and we expect a similar temperature overestimation for Al–Cu alloys here of ~200–250 °C. Therefore, in all the calculated results below, we apply this ad hoc temperature correction, and compare our calculated results to experimental data at precipitation temperatures of interest of ~200–250 °C.

In a phase-field model, homogeneous nucleation can be modeled by either adding random thermal noises in the Cahn–Hilliard and Allen–Cahn equations [24,34] or by explicitly introducing nuclei according to the classical nucleation theory applied locally in a system [35,36]. Since the main focus of this paper is on the growth and coarsening process of precipitates rather than the nucleation, the precipitates were simply introduced at random locations. As smaller particles are more strongly controlled by interfacial energies (relative to strain energies) than large ones, the initial conditions in all our simulations correspond to randomly distributed nuclei of θ' with an aspect ratio ~3:1, based on first-principles calculated interfacial energy anisotropy.

5. Results: phase-field modeling

5.1. Equilibrium morphology of θ'

In an effort to understand the physics controlling the equilibrium morphology of θ', we have calculated morphologies from our multiscale approach, including various physical factors which affect the precipitate morphology, both individually and in combination. Fig. 9 is a collection of the late stage precipitate microstructures obtained from phase-field simulations with different combinations of energetic contributions: (i) isotropic interfacial energy alone, (ii) anisotropic interfacial energy alone, (iii) anisotropic strain (or elastic energy) alone, and (iv) the "full" calculations using both anisotropic interfacial and elastic energy in combination. The simulation results for these four cases are compared with an experimental TEM micrograph of a 319-type Al–Si–Cu alloy aged at ∼230 °C for 3 h [37]. Though all the simulations started with similar initial conditions, the number of precipitates in the microstructure in the late stages is dependent on the anisotropy contribution(s) included. In general, the presence of strain increases the critical nuclei size and hence, reduces the number of precipitates which attain the growth stage. Also, some coalescence effects are observed (in the case of elastic energy anisotropy) from closely spaced identical precipitate variants which survived to the growth stage.

(i) *Isotropic interfacial energy alone:* As expected, the resulting precipitate shapes are spherical with increase in average precipitate size caused by growth and coarsening. (ii) *Anisotropic interfacial energy alone:* The precipitates are plate-shaped with an aspect ratio close to the interfacial energy anisotropy value of 3. We note that there exists a small effect from spatial discretization of our phase-field model on the morphology. The difference in interfacial widths along the semi-coherent and coherent interfaces, introduced by the anisotropy in interfacial energy, requires a very fine grid spacing to eliminate this spatial discretization artifact completely. The finer grid spacing implies more computational effort in evaluating the model. Hence, we strike a balance between the discretization artifact and the computational effort, and choose a grid spacing such that the precipitate aspect ratio is close to the expected value from interfacial energy anisotropy. Use of an adaptive grid spacing could also be beneficial in eliminating this discretization artifact, and future work in that area would be of interest. (iii) *Anisotropic elastic energy alone:* The elastic energy anisotropy arises from the tetragonality in strain and should result in lens-shaped precipitates [22]. The deviation from the expected lens-shape of precipitates (in Fig. 9(c)) is caused by the coalescence events from neighboring precipitates. (iv) *Anisotropic interfacial and elastic energy in combination:* Only in this case, (Fig. 9(d)), does the model result in θ' precipitates with aspect ratios that are in reasonable agreement with those observed experimentally after long aging times [38]. The experimental TEM micrograph in Fig. 9(e) obtained from a 319-type Al–Si–Cu cast alloy after aging at 230 °C for 3 h is shown for comparison [37]. By determining the effect of different anisotropy contributions on the morphology of θ' precipitates using the multiscale tool, and by comparing with the existing experimental results on equilibrium aspect ratio, we
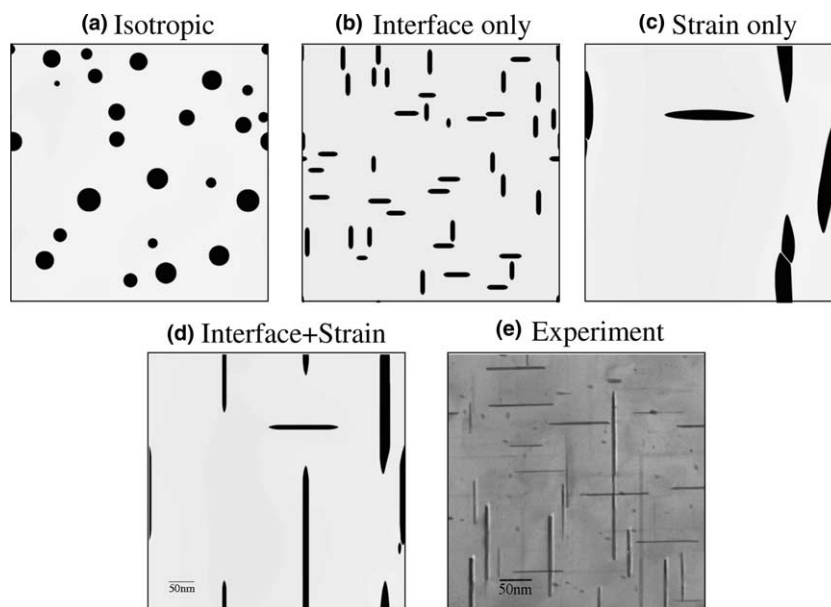

Fig. 9. Phase-field simulation using thermodynamic parameters from first-principles, showing θ' morphologies obtained with different anisotropic contributions for an aging temperature of 200–250 °C. The experimental micrograph is from an Al–Si–Cu cast alloy aged at 230 °C for 3 h [37]. The label on the top of each frame indicates the anisotropy(ies) included (expressed as semi-coherent:coherent; interface – ∼3:1, strain – −0.051: +0.007).
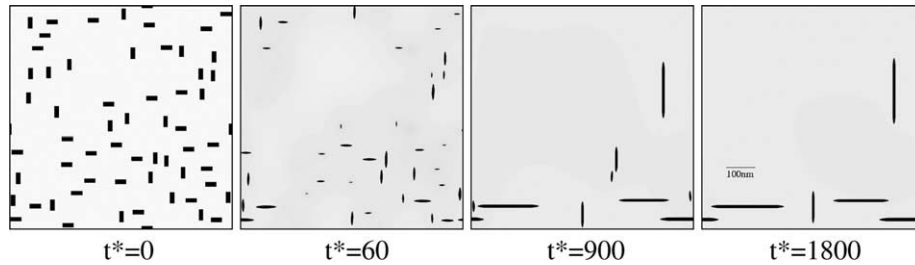
Fig. 10. Microstructure evolution as a function of dimensionless time (t^*) for Al–2%Cu alloy. The simulation size is $\sim750 \times 750$ nm^2.

arrive at the conclusion that the equilibrium precipitate morphology is governed not solely by the interfacial energy anisotropy (as it has been widely believed), nor by the strain energy anisotropy, but rather by a combination of the anisotropies.

5.2. Evolution of multi-precipitate systems

We next turn to applications of our multiscale model to the 2D simulation of microstructural evolution in systems with multiple precipitates. Both interfacial and elastic energy anisotropies are incorporated in all results. The values of dimensionless quantities M^* and t^* used in the simulation, along with the knowledge of diffusion coefficient at the aging temperature (D), characteristic length scale (l) and characteristic free energy (Δf) used in the simulation, provide a simple relation to calculate the real time (t) from the simulation time (t^*). Based on the diffusion coefficient D at the aging temperature and the alloy composition ($\bar{c}$), mobility M is evaluated using an averaged mobility expression [$M = D\bar{c}(1 - \bar{c})$]. With a knowledge of the estimated mobility M, M^* and l, the kinetic parameter L is determined using Eq. (14). The real time is related to t^*, L and Δf through a simple relationship (from Eq. (13))

$$t = \frac{t^*}{L\Delta f}. \tag{28}$$

As an example, the simulation time of $t^* = 900$ for the result shown in Fig. 9(d), corresponds to a real time of ~10 h, based on estimated diffusion coefficient of 10^{-18} m^2/s [39] at 200 °C.

The results discussed in this section are for an alloy with 2% Cu (all compositions expressed in atomic %, unless explicitly stated). The precipitate growth and coarsening of this alloy as a function of time is shown in Fig. 10. A simulation time of 1800 for this alloy corresponds to ~60 h of aging, at 200 °C. The size of the simulated microstructure in Fig. 10 is $\sim750 \times 750$ nm^2.

The number of precipitates that survive the growth stage is only a small percent of the initial number of heterogeneous nuclei, because of the small supersaturation of the alloy. The thickness and length of the plate-shaped precipitates during the evolution vary depending on whether they are growing or shrinking, and on the

interaction with the diffusion fields from neighboring precipitates. When the diffusion fields of the two adjacent precipitates which belong to the same crystallographic variant (same η_p, sign and magnitude) interact, reduction in the interfacial energy favors their coales-
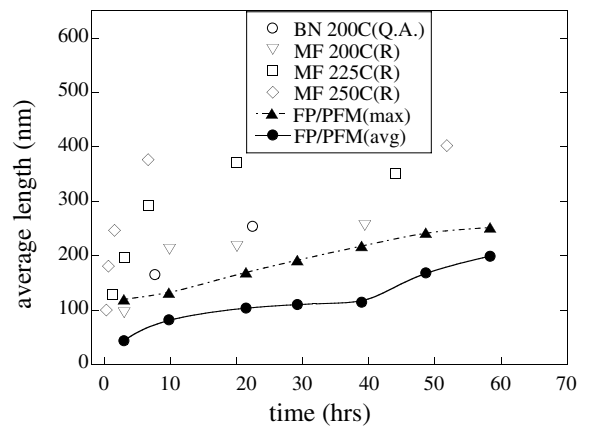

Fig. 11. Average and maximum precipitate length from the multiscale model (FP/PFM – *first-principles phase-field model*) for an Al–2%Cu alloy are compared with average length values from aging experiments of Boyd and Nicholson [6] (BN) and Merle and Fouquet [38] (MF). 'Q.A.' represents quenching and aging after solutionizing (conventional aging), while 'R' represents reversion treatment.
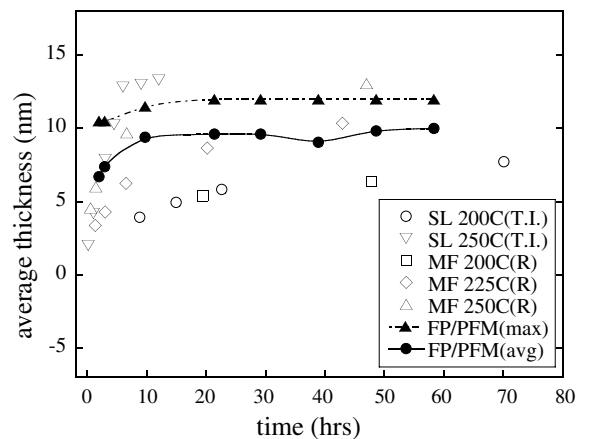

Fig. 12. Average and maximum precipitate thickness from Al–2%Cu alloy compared with the experimental measurements of Sankaran and Laird [40] (SL) and Merle and Fouquet [38] (MF). 'T.I.' represents isothermal treatment, which implies direct isothermal aging after solutionizing without quenching to reduce the density of precipitates and hence, the diffusion field overlaps.
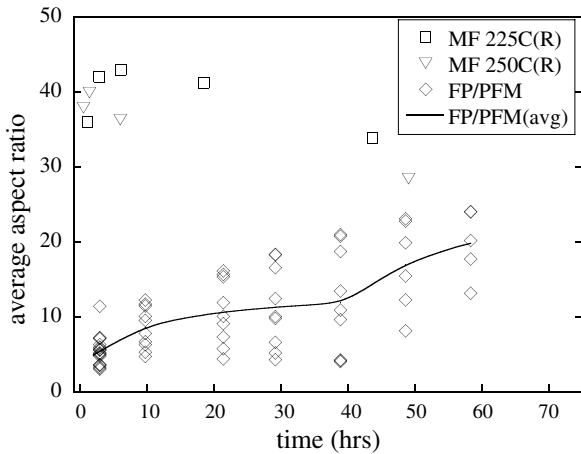
Fig. 13. Average aspect ratio of θ' precipitates from the Al–2%Cu alloy is compared with the experimental results of Merle and Fouquet [38]. The individual aspect ratios from the simulation (FP/PFM) are displayed along with the average aspect ratio in solid line. The equilibrium aspect ratio from the simulation results is in good agreement with the late stage equilibrium value from the experiments.

cence. Also, the same interaction resists coalescence between unlike variants (which would result in an antiphase domain boundary or twin boundary formation) and inhibits their growth, similar to the experimental observations [6,30].

From our simulations of microstructural evolution (Fig. 10), we have extracted quantitative precipitate features like the thickness, length and aspect ratio as a function of time. The thickening and lengthening kinetics obtained from an Al–2%Cu alloy are shown in Figs. 11 and 12. These multiscale modeling (FP/PFM – first-principles phase-field model) kinetics are compared with experimental results available from the literature for precipitation temperatures between 200 and 250 °C. The average (solid line) and maximum (dotted line) values of

length and thickness from the simulation are compared with average values from experiments. It should be pointed out that the experimental measurements selectively measure a few hundred precipitates from the large number of available precipitates. Also, experimental images (in TEM) can include precipitate overlap, which can result both in an overestimation of the average length and also in difficulties in resolving thicknesses at the nanometer-scale, leading to large uncertainties in these measurements. From Figs. 11 and 12, it is clear that the thickness values from our simulations are in closer agreement with experimental results than are the values of precipitate length. We assert that the source of the discrepancy in the case of precipitate length is due to the pronounced interfacial mobility anisotropy and therefore, the much longer non-equilibrium lengths in experimental measurements as compared to the equilibrium values predicted by the simulation. The average aspect ratio of θ' precipitates in the 2%Cu alloy predicted from our simulation (see Fig. 13) agrees well with the measurements of Merle and Fouquet [38], who obtained data after long aging times (a few hundred to a thousand hours). The maximum value of equilibrium aspect ratio from the model predictions does not exceed 30, whereas large non-equilibrium values are observed during aging experiments, presumably induced by the interfacial mobility anisotropy.

The multiscale model can also be used to study and compare the precipitation kinetics of alloys with different precipitate volume fractions. As an example, the precipitate morphology and aspect ratios are compared for three different alloy compositions, 2%, 3% and 4% Cu. The smallest composition studied (2%) is the closest to the Cu compositions in many binary and multicomponent Al–Cu-based alloys of practical interest. Although the higher volume fractions might be somewhat unrealistic, they are important, as they provide
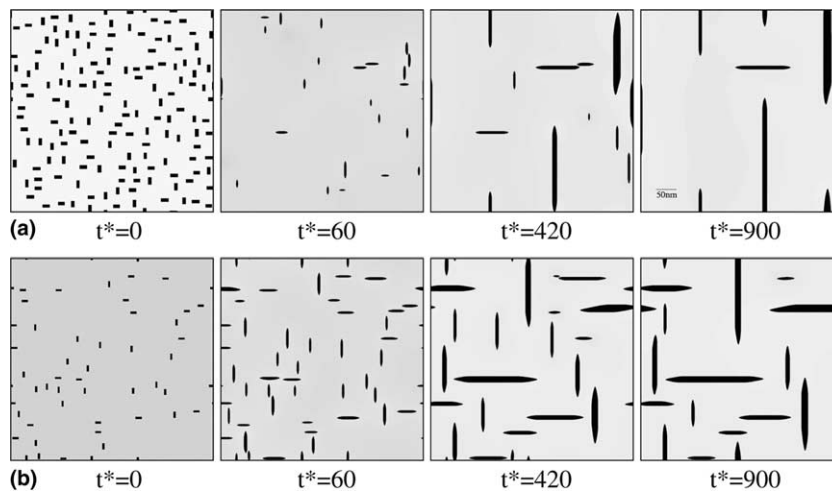

Fig. 14. Precipitate evolution as a function of dimensionless time for (a) Al–3%Cu and (b) Al–4%Cu alloy. $t^* = 900$ corresponds to a real time of $\sim$10 and $\sim$7.5 h for a 3% and 4% alloy, respectively, while for the 2% alloy in Fig. 10, it corresponds to 30 h.
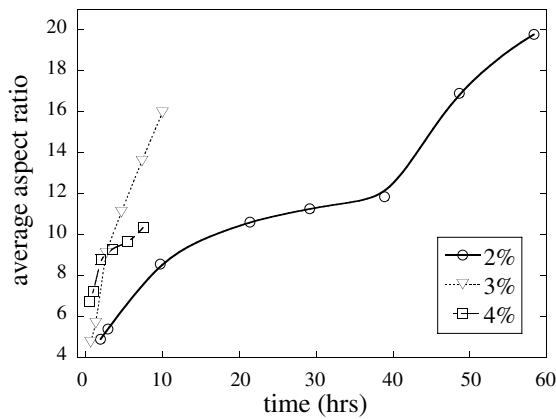
Fig. 15. Average aspect ratio evolution as a function of time compared for the Al–Cu alloys of three different compositions. The aspect ratio seems to decrease slightly with increase in composition, similar to the experimental results of Merle and Fouquet [38].

information necessary to compare the effect of volume fraction on growth/coarsening kinetics.

From the precipitate microstructure evolution in Figs. 10, 14(a) and (b) (corresponding to 2%, 3% and 4% Cu compositions, respectively), it is obvious that the number of precipitates which reach the growth stage from the nuclei stage increases with supersaturation and therefore, results in a larger precipitate density in the late stages of simulation. The real times for the evolution study corresponding to $t^* = 900$ are ~10 and 7.5 h for the 3% and 4% Cu compositions (due to difference in mobility M as a function of alloy composition), respectively, and the simulation size is ~500×500 nm^2. The average aspect ratio of θ' precipitates decrease with increase in alloy composition (2–4% Cu) (see Fig. 15). This type of behavior is also observed in experiments [38], in which the reduction in aspect ratio with increase in alloy composition or supersaturation is caused by enhanced thickening.

The multiscale model helps in understanding the physics behind the equilibrium θ' precipitate morphology. The quantitative predictions of equilibrium aspect ratio of θ' precipitates are in good agreement with experiments. In order to obtain a complete understanding of the non-equilibrium precipitate morphologies in experiments arising from interfacial kinetic anisotropy, a more sophisticated phase-field model that includes misfit defects and accounts for the ledge growth nature of the coherent interface of θ' precipitates, is required.

6. Summary

A multiscale approach is presented to study the precipitate morphology of θ' precipitates in Al–Cu alloys. All of the energetic contributions required by the mesoscale phase-field (bulk, interfacial, and strain) are provided by atomic-scale first-principles calculations combined with cluster expansion and MC techniques. First-principles calculations provide the first reliable interfacial energy and misfit strain values for the coherent and semi-coherent interfaces of θ'. From the multiscale simulation results, we demonstrate that the equilibrium plate-shaped morphology of θ' is not solely governed by interfacial energy anisotropy as believed prevalently, but by the combination of interfacial and elastic energy anisotropies. The time evolution of the equilibrium precipitate features such as the length, thickness, and aspect ratio predicted by the simulation agrees qualitatively with the experimental observations, despite the fact that the model does not account for the non-equilibrium interfacial mobility anisotropy effects. We note that the first-principles/phase-field method proposed here is completely general and is not confined to the θ'/Al case. It should be applicable to a wide variety of problems in microstructural evolution.

References

[1] Wolverton C, Ozolins V. Phys Rev Lett 2001;86:5518.
[2] Hardy HK. J Inst Met 1951;79:321.
[3] Hardy HK. J Inst Met 1953;82:236.
[4] Laird C, Aaronson HI. Trans Metall Soc AIME 1968;242:1393.
[5] Hornbogen E. Aluminium 1967;43:115.
[6] Boyd JD, Nicholson RB. Acta Metall 1971;19:1379.
[7] Doherty RD. Diffusive transformations in the solid state. In: Cahn RW, Haasen P, editors. Physical metallurgy. Amsterdam: Elsevier; 1996. p. 1363–505.
[8] Stobbs WM, Purdy GR. Acta Metall 1978;26:1069.
[9] Mitlin D, Radmilovic V, Morris Jr JW. Metall Mater Trans A 2000;31:2697.
[10] Vaithyanathan V, Wolverton C, Chen LQ. Phys Rev Lett 2002;88:125503.
[11] Chen LQ. Annu Rev Mater Res 2002;32:113.
[12] Ceperly DM, Alder BJ. Phys Rev Lett 1980;45:566.
[13] Perdew JP, Zunger A. Phys Rev B 1981;23:5048.
[14] Perdew JP. In: Ziesche P, Eschrig H, editors. Electronic Structure of Solids, vol. 11. Berlin: Akademie Verlag; 1991.
[15] Singh DJ. Planewaves, pseudopotentials, and the LAPW method. Boston: Kluwer Academic Publishers; 1994.
[16] Kresse G, Furthmuller J. Comput Mater Sci 1996;6:15.
[17] Laks DB, Ferreira LG, Froyen S, Zunger A. Phys Rev B 1992;46:12587.
[18] Wolverton C. Philos Mag Lett 1999;79:683.
[19] Ozolins V, Wolverton C, Zunger A. Phys Rev B 1998;57:6427.
[20] Braun RJ, Cahn JW, McFadden GB, Wheeler AA. Philos Trans R Soc Lond A 1997;355:1787.
[21] Chen LQ. Phase transformation and evolution in materials. In: Proceeding of TMS Symposium; 2000. p. 209–20.
[22] Khachaturyan AG. Theory of structural transformations in solids. New York: Wiley; 1983.
[23] Li DY, Chen LQ. Acta Mater 1998;46:2573.
[24] Elder K. Comput Phys 1993;7:27.
[25] Chen LQ, Shen J. Comput Phys Commun 1998;108:147.
[26] Muller S, Wang L-W, Zunger A, Wolverton C. Phys Rev B 1999;60:16448.
[27] Ozolins V, Wolverton C, Zunger A. Phys Rev B 1998;57:4816.
[28] Aaronson HI, Laird C. Ford Motor Co. Scientific Laboratory Report; 1967.
[29] Weatherly GC. Acta Metall 1971;19:181.

[30] Weatherly GC, Nicholson RB. Philos Mag 1968;17:801.

[31] Dahmen U, Westmacott KH. Phys Stat Sol (a) 1983;80:249.

[32] Cahn JW, Hilliard JE. J Chem Phys 1958;28:258.

[33] Ozolins V, Asta M. Phys Rev Lett 2001;86:448.

[34] Gunton JD, Miguel MS, Sahni PS. The dynamics of first-order phase transitions. In: Domb C, Lebowitz JL, editors. Phase transitions and critical phenomena. New York: Academic Press; 1983. p. 267–466.

[35] Simmons JP, Shen C, Wang Y. Scr Mater 2000;43:935.

[36] Gránásy L, Börzsönyi T, Pusztai T. Phys Rev Lett 2002;88:206105.

[37] Weakley SC, Donlon W, Wolverton C, Jones JW, Allison JE. unpublished.

[38] Merle P, Fouquet F. Acta Metall 1981;29:1919.

[39] Aaronson HI, Laird C. Trans Metall Soc AIME 1968;242:1437.

[40] Sankaran R, Laird C. Acta Metall 1974;22:957.